

# Discovery of New Plasmonic Metals via High-Throughput Machine Learning

Ethan P. Shapera and André Schleife\*

The field of plasmonics aims to manipulate and control light through nanoscale structuring and choice of materials. Finding materials with low-loss response to an applied optical field while exhibiting collective oscillations due to intraband transitions is an outstanding challenge. This is viewed as a materials selection problem that bridges the gap between the large number of candidate materials and the high computational cost to accurately compute their individual optical properties. To address this, online databases that compile computational data for numerous properties of tens to hundreds of thousands of materials are combined with first-principles simulations and the Drude model. By means of density functional theory (DFT), a training set of geometry-dependent plasmonic quality factors for  $\approx 1000$  materials is computed and subsequently random-forest regressors are trained on these data. Descriptors are limited to symmetry, quantities obtained using the chemical formula, and the Mendeleev database, which allows to rapidly screen 7445 candidates on Materials Project. Using DFT to compute quality factors for the 233 most promising materials, AlCu<sub>3</sub>, ZnCu, and ZnGa<sub>3</sub> are identified as excellent potential new plasmonic metals. This finding is substantiated by analyzing their electronic structure and interband optical properties in detail.

## 1. Introduction

In metals, charge carriers can be excited by visible wavelength light to form collective oscillations and intraband transitions near the Fermi level correspond to plasmon oscillations of the electrons. Once excited, plasmons will either be localized on interfaces due to the finite extent of the metal, forming localized surface plasmon resonances (LSPRs), or propagate along extended interfaces as surface plasmon polaritons (SPPs).<sup>[1,2]</sup> The field of plasmonics seeks to precisely manipulate light at the nanoscale, with promising applications including subwavelength waveguides,<sup>[3,4]</sup> nanoantennas,<sup>[5]</sup> superlenses,<sup>[6]</sup> subwavelength imaging,<sup>[7]</sup> nanocircuitry,<sup>[8,9]</sup> and biosensors.<sup>[10]</sup> Control of such excitations requires consideration of both the material used and the geometry into which it is shaped.

Finding new metals or doped semiconductors which may act as viable candidates for plasmonic applications remains an outstanding problem.<sup>[11]</sup> Filled states

near the Fermi level contribute electrons capable of undergoing plasmon oscillations and empty states above the Fermi level become filled by the intraband transitions. Interband transitions, however, do not contribute to plasmon oscillations and exciting them via photon absorption is a loss mechanism. Hence, a perfect plasmonic metal would have electrons near the Fermi level able to propagate through the material with low intraband loss and no interband transitions. High electrical conductivity is a beneficial characteristic, since it indicates weak scattering of electrons as they propagate through the material, that is, low loss due to electron–electron scattering of conduction electrons.<sup>[1]</sup> However, it is not a sufficient criterion because weak electron–electron scattering does not preclude the possibility of light being absorbed by interband transitions rather than exciting propagating electronic modes along the metal–dielectric interface.<sup>[12]</sup>


A wave optical treatment using Maxwell equations imposes that the real part of the dielectric function due to electronic intraband transitions near the Fermi level is negative.<sup>[1]</sup> This derives from solving Maxwell's equations near the metal–dielectric interface, where continuity of the appropriate components of the electric field and displacement field must be enforced. Further, the electromagnetic mode on the surface must propagate along the interface and decay exponentially with distance

E. P. Shapera  
Department of Physics  
University of Illinois at Urbana–Champaign  
Urbana, IL 61801, USA

A. Schleife  
Department of Materials Science and Engineering  
University of Illinois at Urbana–Champaign  
Urbana, IL 61801, USA  
E-mail: schleife@illinois.edu

A. Schleife  
Materials Research Laboratory  
University of Illinois at Urbana–Champaign  
Urbana, IL 61801, USA

A. Schleife  
National Center for Supercomputing Applications  
University of Illinois at Urbana–Champaign  
Urbana, IL 61801, USA

 The ORCID identification number(s) for the author(s) of this article can be found under <https://doi.org/10.1002/adom.202200158>.

© 2022 The Authors. Advanced Optical Materials published by Wiley-VCH GmbH. This is an open access article under the terms of the Creative Commons Attribution-NonCommercial License, which permits use, distribution and reproduction in any medium, provided the original work is properly cited and is not used for commercial purposes.

DOI: 10.1002/adom.202200158

from the interface. Enforcing these conditions produces the constraints

$$\epsilon_m(\omega_o) \times \epsilon_d(\omega_o) < 0 \quad (1)$$

$$\epsilon_m(\omega_o) + \epsilon_d(\omega_o) < 0 \quad (2)$$

where  $\epsilon_d$  and  $\epsilon_m$  are the dielectric functions of the dielectric and the metal, respectively, at operating frequency  $\omega_o$ . This Maxwell-imposed criterion is often satisfied in metals since the intraband dielectric function within the Drude model automatically satisfies it for all frequencies below the plasma frequency.<sup>[2]</sup> The interband contribution to the dielectric function does not generally satisfy this criterion. In summary, a good plasmonic material then fulfills  $\omega_o < \omega_p$  along with weak interband contributions to the dielectric function. Practical applications would also require that candidate materials be chemically stable and easy to synthesize.

In this work we view controlling plasmonic response to an applied optical field as a materials selection problem. The above criterion of  $\omega_o < \omega_p$  leaves open the question of how much larger than  $\omega_o$  should  $\omega_p$  be. The quality factor of the plasmonic oscillation is maximized by selecting a material with as high a plasma frequency as possible, even into the UV region. Typically used plasmonic metals include Ag ( $\omega_p = 9.0 - 9.6$  eV), Au ( $\omega_p = 8.5 - 9.0$  eV), and Al ( $\omega_p = 12 - 15$  eV).<sup>[1,13,14]</sup> There are also applications in which the plasmonic material is structured to have a surface plasma frequency close to the operating frequency.<sup>[15–18]</sup> In this work, we take a quality-factor-based approach and seek to find large bulk plasma frequency materials. This method can be readily adapted to search for any particular range of plasma frequencies. We also limit computations to finding bulk plasma frequencies as opposed to surface plasma frequencies due to the computational cost of simulating a surface as opposed to the bulk, as well as the complications of choosing which surfaces to simulate.

In order to facilitate and accelerate materials selection, publicly accessible online databases have compiled both experimental and computational data for numerous properties of tens to hundreds of thousands of materials. In particular, the desirable balance of low computational cost and high accuracy of density functional theory (DFT)<sup>[19]</sup> recently lead to projects<sup>[20–23]</sup> that contain structural information and detailed electronic-structure data such as band structures and densities of states for materials that were previously synthesized and are reported, for example, in the Inorganic Crystal Structure Database<sup>[24]</sup> or Novel Materials Discovery (NOMAD) repository.<sup>[25]</sup> DFT-based databases have previously been used to design scintillator materials,<sup>[26]</sup> to study optical effects in calcites,<sup>[27]</sup> to find trends in total energy and enthalpy of formation,<sup>[28]</sup> for Li-ion battery design,<sup>[29]</sup> to screen electrocatalytic materials,<sup>[30]</sup> to identify novel solar-cell absorbers,<sup>[31]</sup> and for materials selection for semiconductor heterojunctions.<sup>[32]</sup>

While databases contain DFT results for crystal structures and electronic band structures, calculations of optical properties such as the dielectric function are usually not available. Here, we employ high-throughput DFT calculations to compute dielectric functions of metals to identify high performance candidates for plasmonic applications. Due to the large number

of materials in such databases (e.g.,  $\approx 60\,000$  total materials in Materials Project as of performing this work) and higher computational cost due to the requirement of much finer Brillouin zone sampling compared to calculating the electronic band structure, it is less feasible to compute optical spectra for every material in a database. Instead, we approach the problem of discovering new high-quality plasmonic metals by employing a machine-learning approach. Optical calculations are carried out for a subset of  $\approx 1000$  materials to find quality factor values for plasmonic oscillations. Subsequently we use easily obtained, physically meaningful parameters as descriptors for each material.<sup>[33]</sup> The descriptors are selected based on physical relevance to the electronic properties of the material, including electrons above noble gas configuration of the constituent atoms, ionic radii, electronegativity of constituent atoms, and unit cell structure.

We employ machine-learning algorithms to find statistical models between the input descriptors and quality factors, and then employ these to rapidly predict quality factors as figures of merit for large databases. For a small number of materials, predicted to have high figures of merit using the machine-learned model, we then perform subsequent DFT simulations to confirm or reject the model predictions. In this work, our procedure identifies three prototypes of plasmonic metals, AlCu<sub>3</sub>, ZnCu, and ZnGa<sub>3</sub>, and we also examine element-wise family substitutions. By making element-wise substitutions, the plasmonic response is more finely tuned and can be optimized for specific applications on a case-by-case basis. This partially compensates for the limited accuracy of the predictions from machine learning and partially facilitates studying element-wise substitutions that are close in descriptor space. Furthermore, to better understand relative contributions toward quality factors, we separately discuss the intraband and interband dielectric functions of Ag and AlCu<sub>3</sub>. We find that both the interband and intraband contributions are necessary to capture the quality factor thoroughly. While it is known that interband contributions need to be small for a good plasmonic material, we show from this data that they cannot be neglected when evaluating quality factors and that it is not accurate to approximate the optical response of a metal using only the Drude model and plasma frequency.

## 2. Computational Approach

### 2.1. Optical Response

The response of a metal to an optical field is determined by the electronic inter- and intraband transitions captured by the dielectric tensor. Interband transitions consist of zero-momentum-transfer excitations of an electron from a filled valence to an empty conduction state. This vertical excitation process corresponds to absorption of light, acting as a loss mechanism for plasmonics. Intraband transitions result from light-induced oscillations of electrons near the Fermi energy.

The starting point for describing the intraband optical response of bulk plasmonic metals in both experiment<sup>[12,13,34,35]</sup> and computation<sup>[36–38]</sup> is the Drude model of free carriers under an applied optical field. The Drude model approximates

the charge carriers in a material as a classical free-electron gas. When plane wave light is shone on a metal–dielectric interface, the electric field component parallel to the interface,  $\mathbf{E}_{\text{ext}}$ , excites electronic oscillations along the surface. Oscillations of such carriers at point  $\mathbf{r}$  are described by the equation of motion  $m\dot{\mathbf{r}} = e\mathbf{E}_{\text{ext}} - \gamma\dot{\mathbf{r}}$ , where  $m$  is the effective mass,  $e$  the signed charge, and  $\gamma$  a material-specific damping parameter. The bulk flow of electrons gives rise to a surface current,  $\mathbf{j} = nev$ , and through Ohm's law, the medium has a Drude conductivity,

$$\sigma = \frac{ne^2\tau}{m(1 - i\omega\tau)} \quad (3)$$

with DC conductivity  $\sigma_{\text{DC}} = \frac{ne^2\tau}{m}$  and electron relaxation time  $\tau$ . From the Drude conductivity, the dielectric function of the material due to intraband electronic transitions is

$$\epsilon_{\text{intra}}(\omega) = 1 + \frac{4\pi i\sigma(\omega)}{\omega} = 1 - \frac{\omega_p^2\tau}{i\omega + \omega^2\tau} \quad (4)$$

where  $\omega_p^2 = \frac{4\pi ne^2}{m}$  is the plasma frequency of the carriers. The relaxation time  $\tau$  includes contributions from electron–electron scattering, electron–phonon scattering, and defects. It is possible to calculate the phonon<sup>[39]</sup> contribution to the electron relaxation time with DFT and the electron–electron<sup>[40]</sup> contribution with a Green's function approach.<sup>[41]</sup> However, the experimentally measured electronic relaxation time additionally strongly depends on the grain size of the sample.<sup>[42–44]</sup> Explicitly simulating this process is too computationally expensive to apply to a large number of materials and experimentally dependent on specific samples. Instead, we follow Kumar et al.<sup>[37]</sup> and Zhang et al.<sup>[45]</sup> who address this issue by setting  $\tau$  to a single physically reasonable value, 10 and 80 fs, respectively. As the experimental relaxation times of Ag, Au, and Cu are on the order of 10 fs,<sup>[12]</sup> this value is selected as the relaxation time in this work and below we discuss the influence of this approximation.

The parameter  $\omega_p$  is calculated within the framework of DFT using<sup>[46,47]</sup>

$$\omega_{p,\sigma\rho}^2 = \frac{4\pi e^2}{\Omega} \sum_{\mathbf{k}} w_{\mathbf{k}} \left( \frac{\partial E_{n\mathbf{k}}}{\partial k_{\sigma}} \right) \left( \frac{\partial E_{n\mathbf{k}}}{\partial k_{\rho}} \right) \delta(E_{n\mathbf{k}} - E_{\text{F}}) \quad (5)$$

where  $\Omega$  is the unit cell volume,  $e$  the electron charge,  $w_{\mathbf{k}}$  the normalized weight of the point  $\mathbf{k}$  in the Brillouin zone,  $E_{n\mathbf{k}}$  is the energy of the  $n$ th band at  $\mathbf{k}$ , and  $E_{\text{F}}$  is the Fermi energy. Subscripts  $\sigma$  and  $\rho$  indicate the directions along which the applied electric field oscillates and the direction along which electrons oscillate in response, respectively. Our simulation output directly includes this plasma frequency matrix from intraband transitions and we use this to account for electronic excitations described by the Drude model. For cubic crystals,  $\omega_{p,\sigma\rho}^2$  is diagonal with all three elements equal, but in general,  $\omega_{p,\sigma\rho}^2$  can have off diagonal elements, for example, if the unit cell has non-mutually orthogonal lattice vectors. All 24 materials explicitly named in this paper have diagonal plasma frequency matrices and 15 of these have all three diagonal components equal, including Ag, Au, AlCu<sub>3</sub>, Cu, ZnCu,

and ZnGa<sub>3</sub>. Four of the nine remaining materials show differences in the components of  $\omega_p$  of less than 0.5 eV. Following the example of Kumar et al.,<sup>[37]</sup> we take the average value of the diagonal elements as the plasma frequency. Of the materials named in this paper, the most severe breakdown of this approximation occurs for InAu<sub>3</sub> with diagonal components of  $\omega_p$  of 8.72, 6.66, and 7.45 eV.

The contribution of interband transitions between valence and conduction bands to the dielectric function is described within DFT

$$\epsilon_{2,\alpha\beta}(\omega) = \frac{4\pi^2 e^2}{\Omega} \lim_{q \rightarrow 0} \frac{1}{q^2} \sum_{c,\nu,\mathbf{k}} 2w_{\mathbf{k}} \delta(\epsilon_{c,\mathbf{k}} - \epsilon_{\nu,\mathbf{k}} - \omega) \langle \mathbf{u}_{c,\mathbf{k}+e_{\alpha}q} | \mathbf{u}_{\nu,\mathbf{k}} \rangle \langle \mathbf{u}_{c,\mathbf{k}+e_{\beta}q} | \mathbf{u}_{\nu,\mathbf{k}} \rangle^* \quad (6)$$

where  $q$  is the magnitude of the electron momentum change,  $w_{\mathbf{k}}$  is the symmetry  $\mathbf{k}$  point weight, and  $u_{\nu,\mathbf{k}}$  is the periodic part of the Bloch wave function for band  $\nu$  at  $\mathbf{k}$ .<sup>[48]</sup> Indices  $c, \nu$  run over the conduction and valence bands, respectively, and  $e_{\beta}$  are the Cartesian unit vectors.<sup>[48]</sup> The quantity

$$\mathbf{f}_{c,\nu,\mathbf{k}} = \left| \langle \mathbf{u}_{c,\mathbf{k}} | \mathbf{p} | \mathbf{u}_{\nu,\mathbf{k}} \rangle \right|^2 \quad (7)$$

defines the oscillator strength of the optical transition for an electron excited from valence band  $\nu$  to conduction band  $c$  with constant momentum  $\mathbf{k}$  with  $\mathbf{p}$  the momentum operator.<sup>[49,50]</sup> The real part of the dielectric function is obtained by the Kramers–Kronig transformation

$$\epsilon_{1,\alpha\beta}(\omega) = 1 + \frac{2}{\pi} P \left( \int_0^{\infty} \frac{\epsilon_{2,\alpha\beta}(\omega')\omega'}{\omega'^2 - \omega^2} d\omega' \right) \quad (8)$$

In this work, we determine scalar dielectric functions by averaging the diagonal components of  $\epsilon_{1,\alpha\beta}(\omega)$  and  $\epsilon_{2,\alpha\beta}(\omega)$  separately. We compute the total dielectric function of the material by summing that average with the Drude contribution, Equation (4).

## 2.2. Selection Criteria

Determining the suitability of a material for plasmonic applications may be performed by evaluating quality factors as a figure of merit which depends on both the material choice and the nanoscale geometry. Generically, the quality factor is evaluated based on the enhanced local optical field resulting from an applied optical field,

$$Q = \frac{\text{Enhanced } |\bar{E}|}{\text{Incident } |\bar{E}|} \quad (9)$$

The analytic form of  $Q$  depends on the geometry of the metal–dielectric interface. While no analytic expressions are available for complicated cases such as  $\pi$ -shaped nanostructures,<sup>[51]</sup> nanospirals,<sup>[52,53]</sup> and ring resonators,<sup>[54,55]</sup> the quality factor of two major classes of plasmonic devices has been defined analytically. For SPP at an extended planar interface the quality factor is<sup>[34]</sup>

$$Q_{\text{SPP}}(\omega) = \frac{\epsilon_1^2}{\epsilon_2} \quad (10)$$

For local surface plasmon resonances (LSPR) confined to the surfaces of metallic spheres the quality factor is<sup>[34,56]</sup>

$$Q_{\text{LSPR}}(\omega) = -\frac{\epsilon_1}{\epsilon_2} \quad (11)$$

The different equations for the quality factors demonstrate that a single metal will not necessarily be the optimal material for all circumstances.

In this work, we use data available in the Materials Project database,<sup>[57,58]</sup> to identify materials with beneficial plasmonic quality factors. We restrict this search to polymorphs of materials that are energetically stable, by considering the energy above the convex hull as the energy difference between the lowest energy crystal structure for a compound and the structure of interest. Within Materials Project, typical values are smaller than 0.5 eV per atom and we use >0.1 eV per atom to indicate unstable structures.<sup>[57]</sup>

### 2.3. Descriptors and Machine Learning

In order to connect plasmonic quality factors and plasma frequencies to materials by means of machine-learning models, we need to featurize materials using descriptors. Numerous approaches have been proposed and, usually, depend on the specific application. Several commonly used methods include: Coulomb matrices,<sup>[59]</sup> smooth overlap of atomic positions,<sup>[60]</sup> graphical representations,<sup>[61]</sup> and atomistic features.<sup>[33]</sup> We employ an approach similar to Ghiringhelli et al.<sup>[33]</sup> in which material descriptors are constructed using only properties of the constituent atoms. The atomic properties included are: number of *s*-, *p*-, *d*-, and *f*-electrons above noble gas configuration, atomic mass, electronegativity, ionic radii, atomic dipole moments, and atomic radii. Property values are taken from the Mendeleev python library.<sup>[62]</sup> While this allows descriptors to be constructed rapidly from minimal a priori information, this featurization approach suffers from being unable to distinguish different polymorphs. We include consideration of polymorphs through one-hot encoding of the crystal symmetry. We use DFT to calculate explicitly the dielectric functions and plasma frequencies for a training set of 970 randomly selected metals from Materials Project.

Fitting, validation, and testing errors were computed for six common machine-learning algorithms, as well as the inclusion of boosting, available in scikit-learn.<sup>[63]</sup> Among the considered machine-learning algorithms, decision tree regressors with adaptive boosting were found to produce the lowest error models. This approach has the additional benefit of being readily optimized due to the small number of hyperparameters. Constructed models were validated using a two-stage scheme, where 10% of the training set was randomly designated the testing set. The testing set remained fixed throughout validation and model construction. The remaining training data was then divided randomly by 80% into a set for fitting a decision tree regressor and 10% into a validation set. The fit model then

was applied to both the validation and testing sets. The process was repeated for 100 random fitting-validation partitions and values for the testing set are determined by averaging over these. Results are discussed below. Model errors were found to be unchanged with increasing the training set size from 920 materials to 970 materials.

### 2.4. Density Functional Theory

We compute the quality factor training sets using the Vienna Ab Initio Simulation Package (VASP) version 5.3.3.<sup>[46,47]</sup> The exchange-correlation functional used is the generalized gradient approximation (GGA) of Perdew, Burke, and Ernzerhof.<sup>[64]</sup> Materials along with their relaxed crystal structure are chosen from Materials Project with the pymatgen open source library.<sup>[57,58]</sup> For efficiency of these simulations, the training set materials are limited to a maximum of 35 atoms in the unit cell. Optical calculations<sup>[48]</sup> are carried out using a plane-wave cutoff of 550 eV and a  $31 \times 31 \times 31$   $\Gamma$ -centered *k*-point grid. This high *k*-point density is found to be sufficient to obtain a plasma frequency of Au which is stable within a  $\pm 0.1$  eV range.

Quality factors are evaluated from the dielectric functions, including intra- and interband contributions, at energies of 1.1655, 1.9590, and 2.8075 eV. These energies represent operating energies of lasers commonly used for plasmonic applications: Nd:YAG ( $\lambda = 1064$  nm),<sup>[65,66]</sup> HeNe ( $\lambda = 633$  nm),<sup>[67,68]</sup> and HeCd metal vapor ( $\lambda = 442$  nm).<sup>[69,70]</sup> Relevant input and output files, as well as a datafile with the post-processed DFT results for generating the figures in this paper can be found in the Materials Data Facility.<sup>[71-73]</sup>

## 3. Results and Discussion

### 3.1. Plasma Frequency

As discussed above, in order for a metal-vacuum interface to allow an oscillating mode, the operating frequency  $\omega_0$  must be below the plasma frequency of the metal  $\omega_p$ .<sup>[1,2]</sup> Hence, candidate materials for plasmonics can be downselected in an initial filtering step by requiring the plasma frequency to be much greater than the operating frequency of a given application. For such considerations and as validation of the concept, we first construct and validate a machine-learned model for plasma frequencies of metals.

First, we minimize the decision tree regressor model training errors by optimizing the maximum tree depth hyperparameter. Maximum decision tree depths are varied between four and ten layers and **Figure 1** shows the corresponding fitting, validation, and testing mean absolute errors (MAEs). The distribution of  $\omega_p^{\text{DFT}}$  values used in training is shown in **Figure 2**. The fitting MAE decreases monotonically with increasing tree depth, which we attribute to the increasing number of fitting parameters. The testing set MAE shows a minimum at a maximum tree depth of 6. For maximum tree depths below 6, there are no sufficient number of fitting parameters to capture the relation between the descriptors and  $\omega_p$ . However, allowing tree



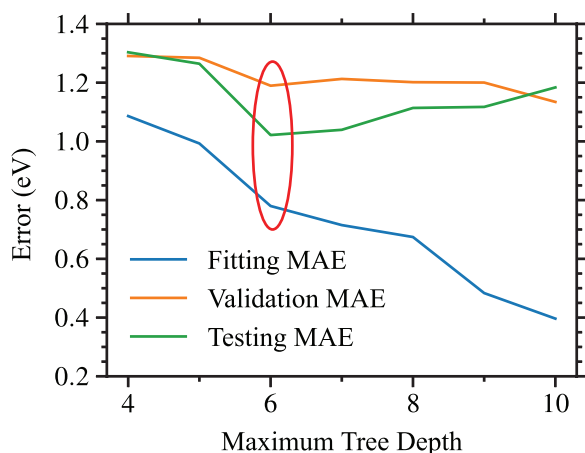


**Figure 1.** Hyperparameter optimization of the decision tree regressor for obtaining the best plasma frequency model. Based on fitting, validation, and testing errors, we restrict the maximum tree depth to six. This depth corresponds to a local minimum in the validation mean absolute error (MAE) and the global minimum of the testing MAE. As the maximum depth is increased beyond six layers, the fitting MAE continues to decrease while the testing MAE becomes larger.

depths greater than 6 leads to more severe overfitting, which manifests itself in the decreasing fitting set MAE, while the testing MAE increases.

A decision tree regressor with adaptive boosting is trained on DFT-calculated plasma frequencies and comparison of the machine-learned and DFT-calculated plasma frequencies for the metal training set is shown in **Figure 3**. The model produces MAEs of 0.78 eV for the fitting set, 1.2 eV for the validation set, and 1.0 eV for the testing set. This indicates that with the optimum choice of the maximum tree depth hyperparameter, overfitting is still present: The validation and testing MAEs are approximately factors of 1.5 and 1.3 larger than the fitting MAE, respectively. However, while the validation and testing MAEs are larger than the fitting MAE, they are still close enough to produce a usable model.

The decision tree regressor model produces non-Gaussian distributions of fitting and validation errors in  $\omega_p^{\text{ML}}$ , see **Figure 3b**. This plot shows the differences between

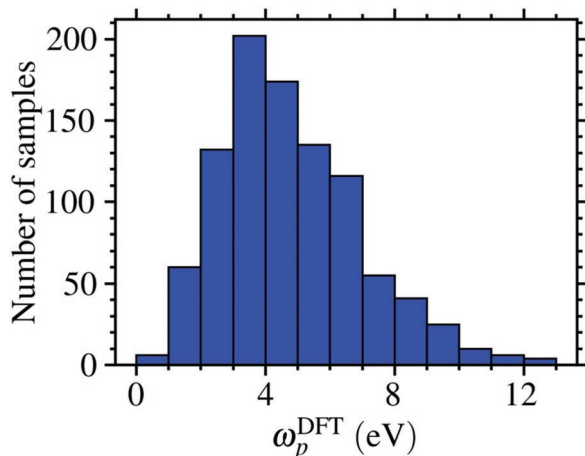


**Figure 2.** Distribution of  $\omega_p^{\text{DFT}}$  for the 970 materials in the training set.

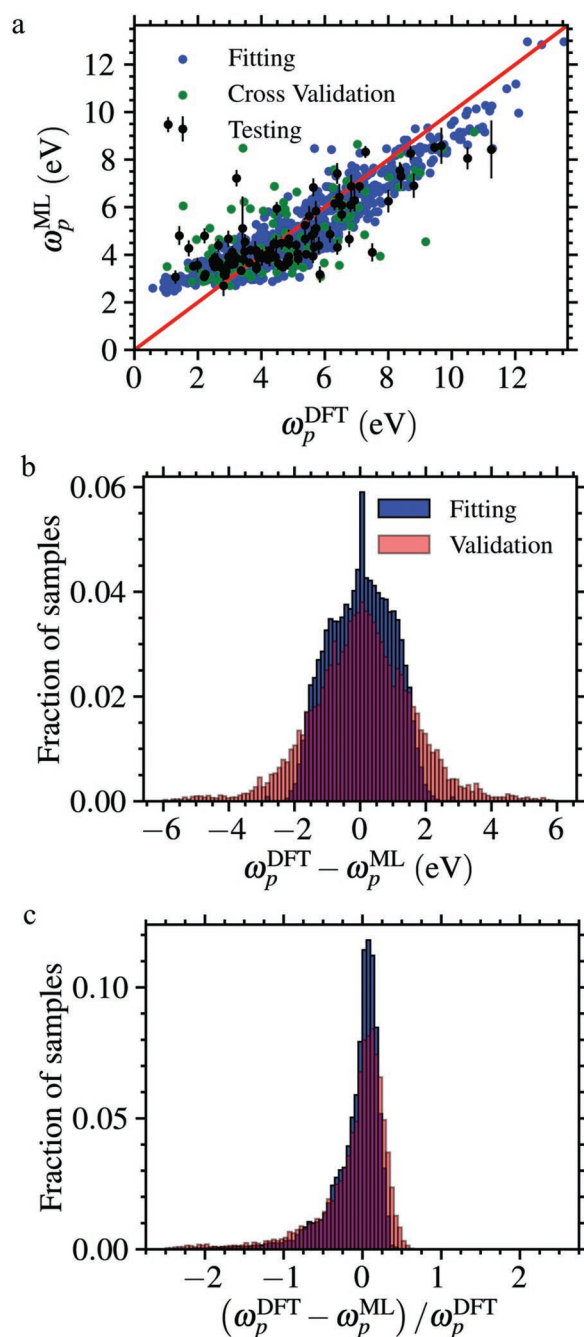


**Figure 3.** a) Comparison of  $\omega_p^{\text{ML}}$ , predicted via the decision tree regressor, and  $\omega_p^{\text{DFT}}$  calculated with DFT. Plotted are the results of one fitting–validation iteration as well as testing set average values and error bars for all 100 iterations. Red line is a guide to the eye. b) Distribution of machine-learning errors of  $\omega_p$  for 100 fitting–validation iterations. The distributions are unimodal and nearly symmetric about their respective means. c) Distribution of machine-learning fractional errors of  $\omega_p$  for 100 fitting–validation iterations. Both distributions are unimodal and negative skewed.

machine-learning-predicted  $\omega_p^{\text{ML}}$  and DFT-calculated  $\omega_p^{\text{DFT}}$  for fitting and validation sets over all 100 fitting–validation iterations. The fitting set shows a mean error of 0.03 eV with 1-standard deviation width of 0.9 eV. The validation set has a

mean error of 0.06 eV with 1-standard deviation width of 1.7 eV. Errors between the DFT-computed and the machine-learning-predicted plasma frequencies show unimodal distributions with skewnesses of 0.06 for fitting and  $-0.15$  for validation. We observe a small bias toward underestimating  $\omega_p^{\text{DFT}}$ , with the constructed model predicting smaller values for 51% of both fitting and validation materials. The unimodal distribution of errors indicates that there is no subgroup of metals for which the model consistently fails.

Further, the Spearman correlation coefficients between the DFT-calculated plasma frequencies and the model-predicted frequencies are calculated as 0.90 for the fitting set and 0.70 for the validation set. Spearman coefficient values near 1.0 indicate that the model will typically correctly order materials by plasma frequency even in instances where the individual values do not match the DFT values.<sup>[74]</sup> The non-Gaussian characters of the error distributions are apparent through the kurtoses of  $-0.75$  for fitting and 1.7 for validation, neither matching the Gaussian kurtosis of 0. Fitting errors are almost entirely confined to between  $-2$  and  $2$  eV, with a negative kurtosis value indicating smaller than Gaussian tails. The validation error distribution is not as tightly confined as the fitting error distribution; there are more large error samples than would be expected for a Gaussian distribution.

By considering the fractional error distributions in Figure 3c bias and non-Gaussianity in the constructed model is further shown. The fitting set shows a mean fractional error of  $-9\%$  and the validation set has a mean fractional error of  $-15\%$ . While the absolute errors show nearly symmetrical distributions, the fractional errors are skewed, with skewnesses of  $-2.8$  for fitting and  $-3.9$  for validation. The skewness manifests as a tail in the fractional error distribution seen for  $\omega_p^{\text{DFT}} < \omega_p^{\text{ML}}$ . The fractional error distribution kurtoses are 14 for the fitting and 23 for the validation set, characteristic of larger than Gaussian tails.

However, the fractional errors are not consistent over the range of metals. While Gaussian distributed fractional errors would require that small plasma frequency materials also have small errors and large plasma frequency materials have large errors, we obtained an error being constant across the range of plasma frequencies and the model has a tendency to overestimate  $\omega_p^{\text{DFT}}$  of low  $\omega_p^{\text{DFT}}$  metals. This causes small plasma frequency materials to tend to have larger fractional errors while high plasma frequency materials have lower fractional errors. The typical size of overestimation in the low  $\omega_p$  metals is consistent with the error seen at large  $\omega_p$  materials, but this translates to large fractional errors in the low  $\omega_p$  materials. However, since for plasmonic applications large  $\omega_p$  is desirable, this error in the low  $\omega_p$  regime is not detrimental to the current study.

In summary, the constructed model is able to predict plasma frequencies of a wide range of metals with approximately Gaussian distributed errors. While the accuracy of the model is limited by the 1.0 eV MAE, which is larger than typical experimental uncertainty of  $\approx 0.5$  eV, its utility arises from the ability to screen rapidly large databases without needing to perform DFT calculations for all metals and using the results to downselect for materials with plasma frequencies near a desired value that fulfill the criterion  $\omega_p \gg \omega_c$ .

### 3.2. Quality Factor Models

In this work we consider two simple material configurations for plasmonics, a planar vacuum–metal interface and metallic nanospheres in vacuum. Separate machine-learning models  $Q_{\text{LSPR}}^{\text{ML}}$  and  $Q_{\text{SPP}}^{\text{ML}}$  are fit for the corresponding quality factors to the DFT-calculated values  $Q_{\text{LSPR}}^{\text{DFT}}$  and  $Q_{\text{SPP}}^{\text{DFT}}$  at each considered energy. As representative examples, Figures 4a and 5a plot the results for one fitting–validation iteration of model construction for  $Q_{\text{LSPR}}^{\text{ML}}$  (1.165 eV) and  $Q_{\text{SPP}}^{\text{ML}}$  (1.165 eV), including the values of one standard deviation error bars for the testing set from all 100 fitting-validation iterations. Both models show clustering of fitting, validation, and testing around the ideal fit of  $Q^{\text{ML}} = Q^{\text{DFT}}$ . However, the models do make a limited number of outlier errors in the testing set for which the DFT-calculated quality factor is not within the one standard deviation error bars. The best agreement between the machine-learning-predicted  $Q^{\text{ML}}$  values for the testing set and the DFT-calculated values occur for smaller  $Q^{\text{DFT}}$ , where there is more training data. At larger values of DFT-calculated quality factors, the machine-learning models tend to underestimate the values.

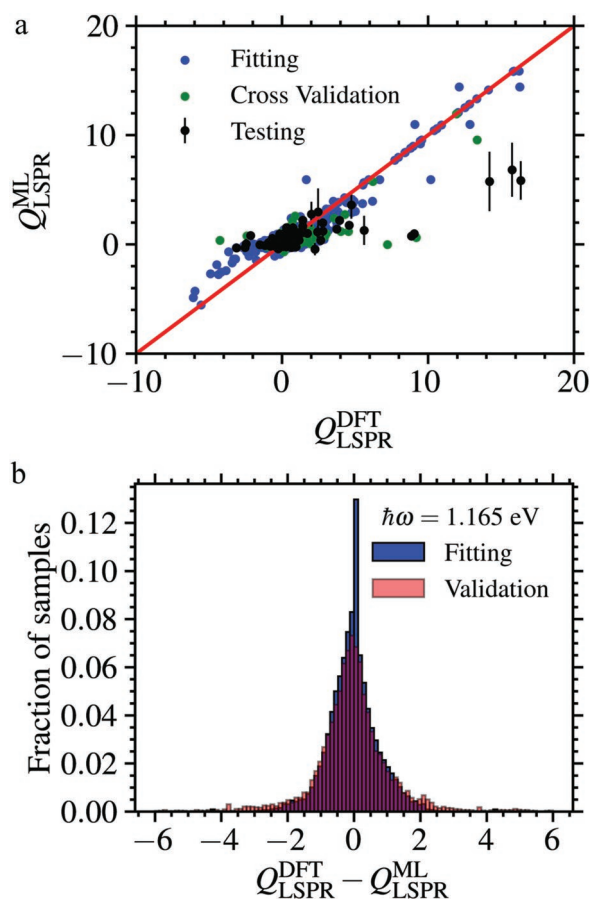


**Figure 4.** a) Comparison of  $Q_{\text{LSPR}}^{\text{ML}}$  predicted via machine-learned regressor versus  $Q_{\text{LSPR}}^{\text{DFT}}$  from DFT. Plotted are the results of one fitting–validation iteration and average values and error bars for all 100 iterations for testing. Red line is a guide to the eye. b) Distribution of differences of DFT-calculated and machine-learning-predicted  $Q_{\text{LSPR}}$  at 1.165 eV for fitting and validation sets.

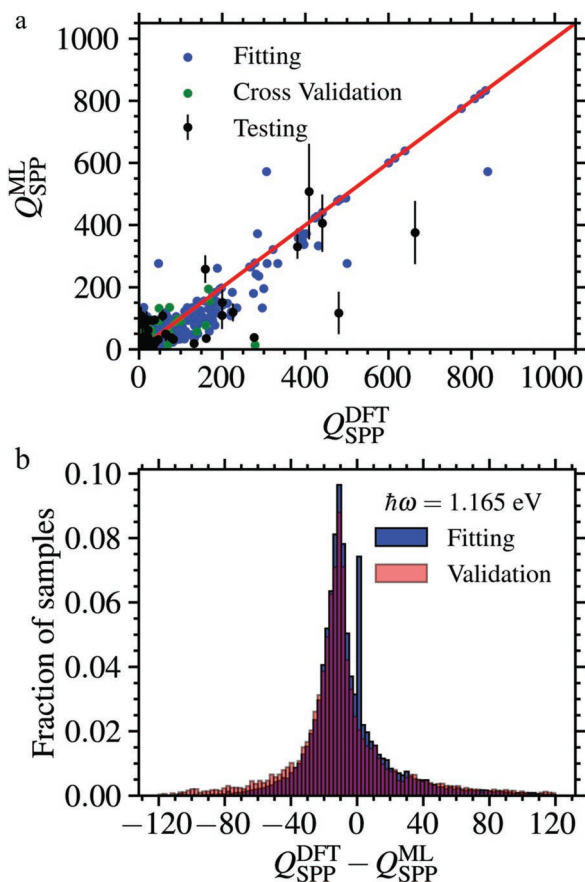


**Figure 5.** a) Comparison of  $Q_{\text{SPP}}^{\text{ML}}$ -predicted via machine-learned regressor versus  $Q_{\text{SPP}}^{\text{DFT}}$  calculated with DFT. Plotted are the results of one fitting–validation iteration and average values and error bars for all 100 iterations for testing. Red line is a guide to the eye. b) Distribution of differences of DFT-calculated versus machine-learning-predicted  $Q_{\text{SPP}}$  at 1.165 eV for fitting and validation sets.

**Table 1** lists the average absolute values of the six examined quality factors and the fitting, validation, and testing MAEs. In all cases, the MAEs are less than the average absolute value of the quality factor, however, the MAEs are within a factor of three. In addition, the absolute errors between the machine-learned model and DFT-computed quality factors show distributions with larger-than-Gaussian tails. This indicates a tendency of the decision tree regressor model constructed here

**Table 1.** MAEs of machine-learned quality factors from initial training set.

Q Factor	$\langle  Q^{\text{DFT}}  \rangle$	Fitting	Validation	Testing
$Q_{\text{LSPR}}^{\text{ML}}$ (1.165 eV)	1.33	0.54	1.00	1.11
$Q_{\text{LSPR}}^{\text{ML}}$ (1.959 eV)	1.07	0.49	0.82	0.86
$Q_{\text{LSPR}}^{\text{ML}}$ (2.807 eV)	0.93	0.43	0.74	0.63
$Q_{\text{SPP}}^{\text{ML}}$ (1.165 eV)	46.5	19.7	38.8	33.8
$Q_{\text{SPP}}^{\text{ML}}$ (1.959 eV)	15.6	6.56	13.7	17.0
$Q_{\text{SPP}}^{\text{ML}}$ (2.807 eV)	9.69	3.66	7.46	5.52

to produce predictions with errors comparable to typical  $Q^{\text{DFT}}$  values, limiting its ability to accurately predict quality factors.

Corresponding plots of the model error distributions are presented in Figures 4b and 5b for  $Q_{\text{LSPR}}^{\text{ML}}$  (1.165 eV) and  $Q_{\text{SPP}}^{\text{ML}}$  (1.165 eV). The fitting error distribution in Figure 4b for the  $Q_{\text{LSPR}}^{\text{ML}}$  (1.165 eV) model is unskewed with an average error of  $-0.03$ , an MAE of 0.54, and a kurtosis of 2.76. Model errors of the fitting set are less tightly clustered about the mean error, with larger-than-Gaussian tails, as indicated by the kurtosis values greater than 0. The validation error distribution for the  $Q_{\text{LSPR}}^{\text{ML}}$  (1.165 eV) model is slightly skewed negatively with an average error of 0.08, MAE of 1.00, and a kurtosis of 15. The skewness in the validation set is sufficiently small and is not visually apparent in Figure 4b. Despite these limitations of the model, there is still a strong correlation between the predicted and DFT quality factors, with a Spearman coefficient of 0.75 between the predicted and calculated values for the fitting set and 0.56 for the validation set. This justifies using our model for downselection.

The error distributions for  $Q_{\text{SPP}}^{\text{ML}}$  (1.165 eV) in Figure 5b are non-Gaussian with larger-than-Gaussian tails and a two-peak distribution of the fitting error. The fitting error is positive skewed with an average error of  $-5.7$ , MAE of 19.7, and a kurtosis of 20. The positive skewness is shown as the average of  $Q_{\text{SPP}}^{\text{DFT}} - Q_{\text{SPP}}^{\text{ML}}$  at  $-5.7$  is larger than the position of the peak in the bin centered at  $Q_{\text{SPP}}^{\text{DFT}} - Q_{\text{SPP}}^{\text{ML}} = -11.25$ . The large kurtosis is attributed to the second peak present in the bin centered at  $Q_{\text{SPP}}^{\text{DFT}} - Q_{\text{SPP}}^{\text{ML}} = 1.25$  and the tails of the distribution. Nevertheless, the SPP models also reproduce the general trend in quality factors with Spearman coefficients between machine-learning and DFT values of 0.62 for fitting and 0.50 for validation. The broad error spread and bimodal distribution of errors indicate difficulty of the model in reproducing the computed relation between the chosen descriptors and  $Q_{\text{SPP}}^{\text{DFT}}$ .

For this work, we did not find it necessary to spend excessive resources developing highly accurate machine-learning models of the plasmonic quality factors. Instead we use a less accurate model which reproduces general trends as a coarse filter and then explicitly check the predictions by performing DFT simulations of dielectric functions. However, we note that several approaches exist for improving machine-learning model accuracy, for example, by using improved descriptors which are more closely related to the target property.<sup>[75]</sup> This includes Mordered<sup>[76]</sup> or rdkit<sup>[77]</sup> descriptor sets that were found to be useful as these are often closely related to physical properties of interest. Including descriptors based on electronic band structure or atomic orbitals may lead to lower error machine-learning models for predicting dielectric-based quality factors. Alternatively, the chosen algorithm of decision tree regressors with adaptive boosting may struggle to find a relationship between the descriptors and the target quantities. Deep learning algorithms, including neural networks, have shown remarkable success predicting physical properties and complex chemical processes.<sup>[78–81]</sup> The success of neural networks arises from the ability to learn nonlinear relations between the descriptors and quantity of interest, but comes at the cost of requiring larger training sets than conventional machine-learning algorithms.<sup>[82,83]</sup>

### 3.3. Predicting New Plasmonic Materials

Due to the prediction errors discussed for the constructed machine-learning models for quality factors in Section 3.2, we use them only to downselect for possible high-quality factor materials from the Materials Project database which had not already been included in the training set. In determining the materials space to search, we begin with the full set of metals available in the Materials Project database. All metals which have been included in the training set are removed because quality factors have already been calculated for these materials using DFT. Two further criteria are imposed to account for ease of fabrication of any potential candidate: the energy above the convex hull must be less than 0.10 eV and the unit cell must contain no more than 20 atoms. This results in a search space of 7445 possible metals and descriptors are calculated for each. The set of metals with their descriptors are fed into the constructed machine-learning models. Predicted values of the plasma frequency and quality factors are determined from the models by averaging over 100 fitting-validation iterations. At this stage, we filter out any metals containing Hg, Pb, Cd, or *f*-block elements. These materials are only removed late in the process in case they contain the only potential high quality factor materials. Combining the machine-learning filtering and fabrication criteria, the 233 potential highest-quality factor metals have been selected for explicit calculation of quality factors using DFT. A flowchart for the selection process is provided in Figure 6.

For these 233 non-radioactive materials, none of which contained Hg, Pb, Cd, or *f*-block elements, we performed DFT simulations and selected three with a simple crystal structure that displayed the largest in one of the six considered quality factors: AlCu<sub>3</sub>, ZnCu, and ZnGa<sub>3</sub>. AlCu<sub>3</sub> is in the Fm $\bar{3}$ m space group with cubic symmetry. ZnCu and ZnGa<sub>3</sub> are in the Pm $\bar{3}$ m space group with cubic symmetry. In the list of 233 materials, we note a lack of metal nitrides, which are subjects of study for plasmonics, for example, by Habib et al.<sup>[84]</sup> Their absence is discussed in Section F, Supporting Information.

In Figure 7 we compare the distribution of predicted and DFT-calculated plasma frequencies for these three metals. The plasma frequency of AlCu<sub>3</sub> is computed as 9.00 eV and predicted by the machine-learned model as  $8.03 \pm 0.38$  eV. For ZnCu, the computed plasma frequency is 9.59 eV, outside the machine-learning  $1-\sigma$  prediction of  $8.57 \pm 0.26$  eV. Also just outside the  $1-\sigma$  prediction of  $9.64 \pm 0.96$  eV, the computed plasma frequency of ZnGa<sub>3</sub> is 10.64 eV.

The constructed plasma frequency model shows a tendency to underestimate  $\omega_p^{\text{DFT}}$  for large plasma frequency metals in the testing set. To explain this, the plot in Figure 2 shows the distribution of plasma frequencies for all materials in the training set used to train our model. Of the 970 included materials, 25 materials have a plasma frequency between 9.0 and 10.0 eV and a further 25 have a plasma frequency above 10.0 eV. Due to the smaller number of training points at large plasma frequencies, our model would be expected to underestimate in this regime, since it was mostly trained on intermediate plasma frequency values. Similarly, we expect that the model would overestimate values at the low end of the range used for training, due to the limited number of training points. If required, the model could

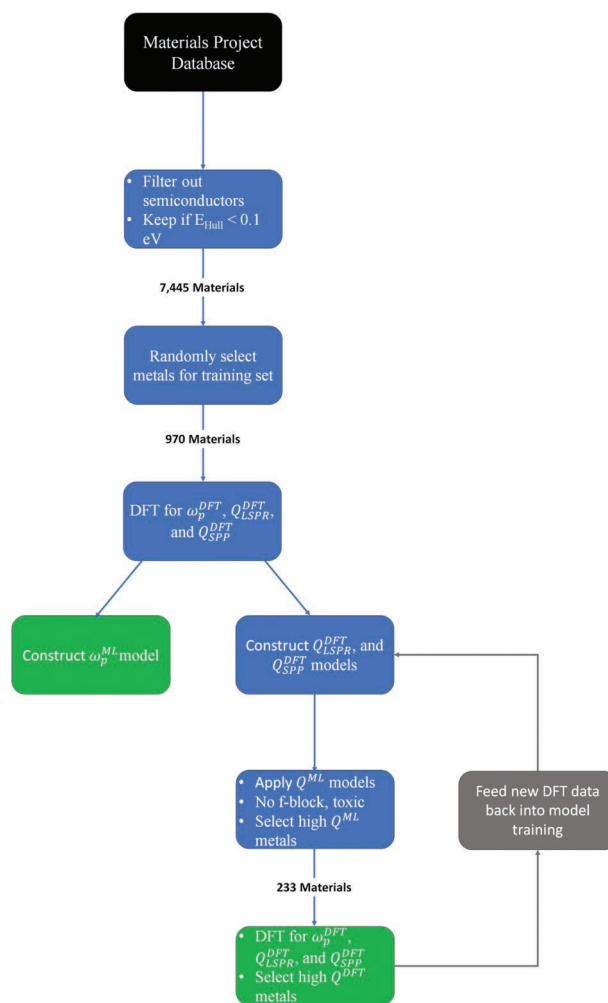


**Figure 6.** Flowchart for constructing machine-learning models and selecting high  $Q^{\text{DFT}}$  metals. In gray is a possible addition to the process for iterative learning to improve the model accuracy for high-quality factor metals. The bottom-most green boxes are the results of the machine-learning process which are reported in this work. DFT simulations have been carried out to verify model predictions represented by the green boxes.

be improved using sequential learning, where potential high or low plasma frequency materials would be identified using the machine-learning model, the corresponding plasma frequencies explicitly calculated in DFT, and then added to the training set in a subsequent model building iteration.

$Q_{\text{LSPR}}^{\text{DFT}}$  and  $Q_{\text{SPP}}^{\text{DFT}}$  for the three selected materials are compared to the commonly used plasmonic noble metals Ag, Au, and Cu in Figure 8. The highest-quality factor material depends on both the energy and the chosen quality factor. No single material has the highest-quality factor at all energies for both  $Q_{\text{LSPR}}^{\text{DFT}}$  and  $Q_{\text{SPP}}^{\text{DFT}}$ . At 1.165 eV Ag and Au have  $Q_{\text{LSPR}}^{\text{DFT}}$  values of 15.8 and 13.4, respectively. The  $Q_{\text{LSPR}}^{\text{DFT}}$  for Au is exceeded by ZnCu (14.2) and closely matched with AlCu<sub>3</sub> (13.2). Ag outperforms both other currently used materials and the predicted new materials at 1.165 and 1.959 eV. With  $Q_{\text{LSPR}}^{\text{DFT}}$  of 1.58 at 1.165 eV, ZnGa<sub>3</sub> underperforms all other materials. At increased energies, however, Au and Cu suffer decrease in  $Q_{\text{LSPR}}^{\text{DFT}}$  and ZnGa<sub>3</sub> becomes



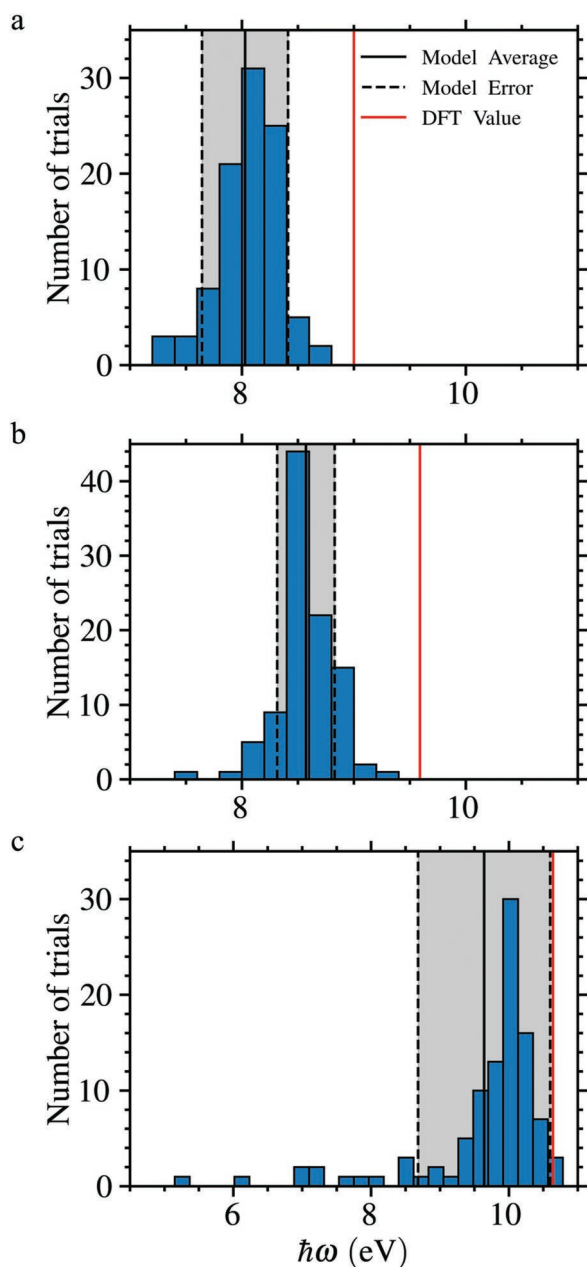


**Figure 7.** Distributions of machine-learning-predicted  $\omega_p$  for a)  $\text{AlCu}_3$ , b)  $\text{ZnCu}$ , and c)  $\text{ZnGa}_3$  computed from averaging 100 fitting-validation iterations.

the highest-quality factor material for both LSPRs and SPPs above 2.8 eV. The sharp decreases in quality factors for Au and Ag correspond to the turning on of interband absorption in this energy range, since Au and Ag both possess direct optical gaps of  $\approx 2.0$  eV (Au) and  $\approx 2.4$  eV (Ag).

While no single material outperforms the current standard plasmonic metals over the full optical energy range,  $\text{AlCu}_3$ ,  $\text{ZnCu}$ , and  $\text{ZnGa}_3$  all outperform Au and Cu for at least one of the six considered quality factor-energy combinations. In particular,  $\text{AlCu}_3$  and  $\text{ZnCu}$  are promising choices for near-IR, with comparable  $Q_{\text{LSPR}}^{\text{DFT}}$  values to the commonly used Au.  $\text{ZnGa}_3$

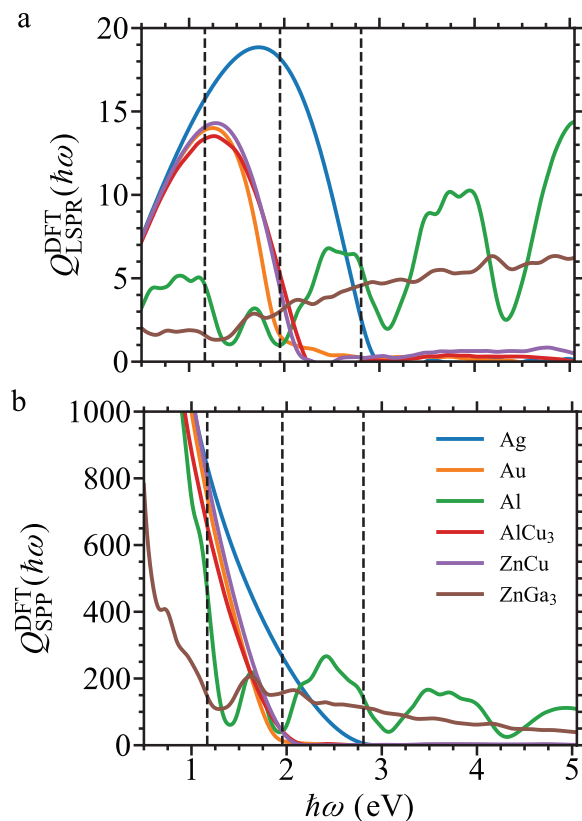


**Figure 8.** a)  $Q_{\text{LSPR}}^{\text{DFT}}$  is plotted for reference materials Ag, Au, and Al, and computed for the new materials  $\text{AlCu}_3$ ,  $\text{ZnCu}$ , and  $\text{ZnGa}_3$ . b)  $Q_{\text{SPP}}^{\text{DFT}}$  is plotted for reference materials Ag, Au, and Al, and computed for the new materials  $\text{AlCu}_3$ ,  $\text{ZnCu}$ , and  $\text{ZnGa}_3$ . Vertical dashed lines correspond to energies of 1.165, 1.959, and 2.807 eV.

has potential to fill the role of a UV plasmonic material. These trends also apply to  $Q_{\text{SPP}}^{\text{DFT}}$ .

In order to provide a deeper understanding of these results, we analyze electronic band structures and projected densities of states of Ag,  $\text{AlCu}_3$ ,  $\text{ZnCu}$ , and  $\text{ZnGa}_3$  in **Figure 9a–d**, and oscillator strengths of the optical transitions for each material in **Figure 10**. The Ag band structure in **Figure 9a** shows a finite density of states near the Fermi level that is required for plasmon oscillations. It also shows an absence of low energy vertical optical transitions below 2.43 eV, see **Figure 10a**, rendering Ag the material with the largest minimum interband optical transition energy of the materials investigated in this paper. This leads to Ag being the metal with highest-quality factors at energies of 1.165 and 1.959 eV.

The band structures and allowed transitions of  $\text{AlCu}_3$  and  $\text{ZnCu}$  show qualitatively similar behavior to Ag. Both materials show a lack of allowed optical interband transitions up to 2 eV, preventing optical absorption loss. Conversely, in  $\text{ZnGa}_3$  low energy optical transitions with large oscillator strengths are allowed, corresponding to strong absorption and low quality factors at low energy. At higher energies, the transition oscillator strengths decrease, leading to  $\text{ZnGa}_3$  weakly absorbing in the UV spectrum. Steeply sloped bands near the Fermi level lead to a large plasma frequency of  $\text{ZnGa}_3$  according to Equation (5), allowing plasmon oscillations at high energies.

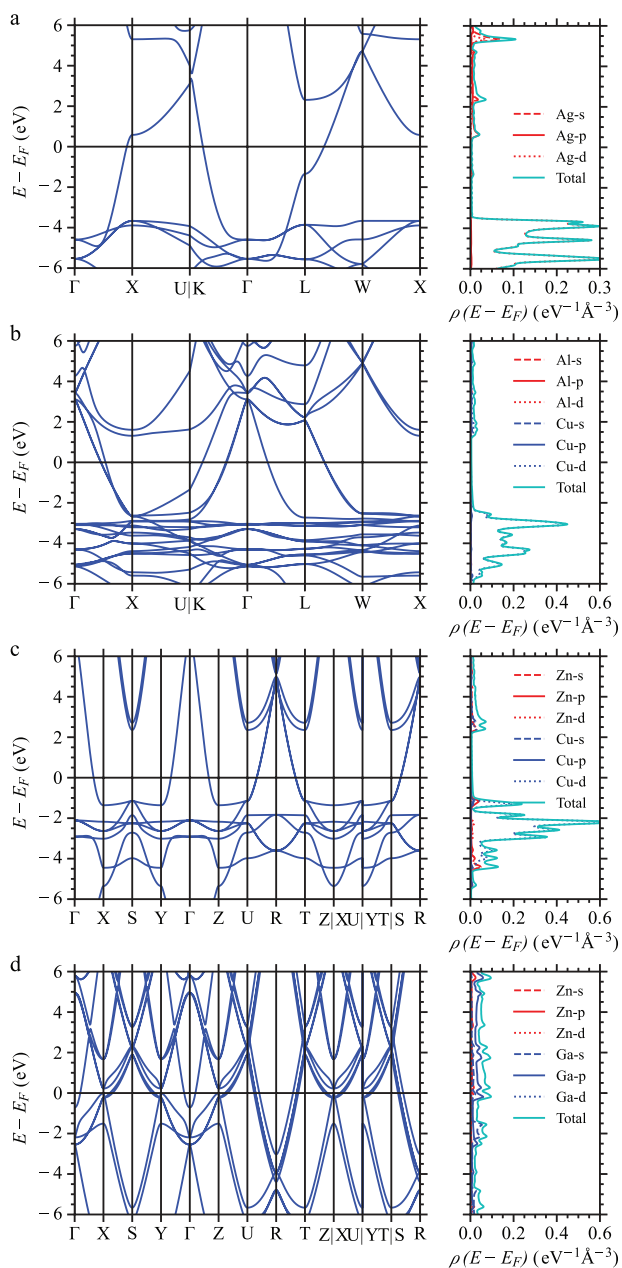


**Figure 9.** Electronic band structure and projected density of states per unit cell volume of a) Ag, b)  $\text{AlCu}_3$ , c)  $\text{ZnCu}$ , and d)  $\text{ZnGa}_3$ . High symmetry  $\mathbf{k}$ -points were selected using Seek-path.<sup>[85,86]</sup>

All DFT calculations in the main text of this work are performed with the PBE exchange-correlation functional within the GGA.<sup>[87]</sup> In metals, using the PBE functional can lead to the  $d$ -bands being placed at the incorrect energies.<sup>[88]</sup> We attempt to correct for the placement by evaluating the quality factors using the HSE06 hybrid exchange-correlation functional.<sup>[89,90]</sup> The results are reported for  $\text{AlCu}_3$  and  $\text{ZnGa}_3$  in Section E, Supporting Information. Using hybrid functionals increases the computational cost by factors of 100 to 1,000. High-throughput use of hybrid functionals in DFT is prevented by the increased computational cost compared to GGA functionals.

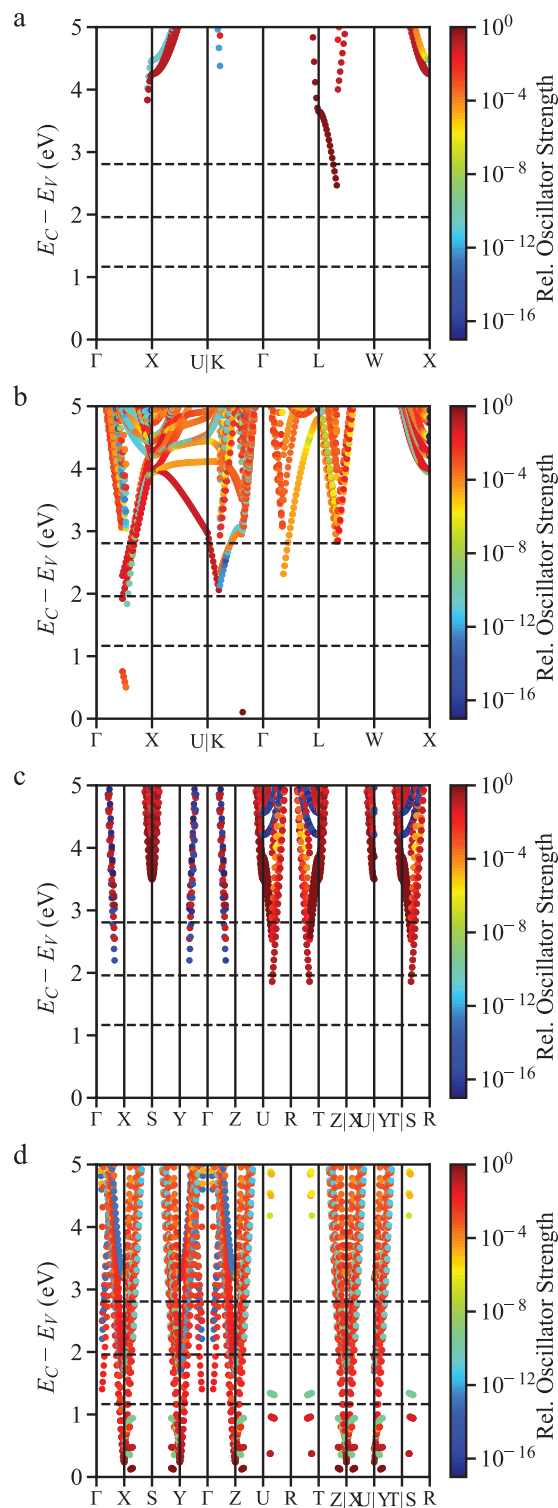


**Figure 10.** Direction-averaged  $\mathbf{k}$ -resolved relative oscillator strengths and energy of the vertical optical transition from valence state  $\nu$  to conduction state  $c$  for a) Ag, b)  $\text{AlCu}_3$ , c)  $\text{ZnCu}$ , and d)  $\text{ZnGa}_3$ . This figure shows relative oscillator strengths, by scaling the individual value from Equation (7) linearly such that the single strongest transition of all four material has a relative oscillator strength of 1. Horizontal dashed lines correspond to energies of 1.165, 1.959, and 2.807 eV.

In selecting materials for plasmonics, we have considered only the quality factors. For practical implementation, more issues must be considered. We carry out several further tests of material viability for AlCu<sub>3</sub>, ZnCu, and ZnGa<sub>3</sub>, and compare against well known plasmonic metals, with results described in the Supporting Information. Device conditions will require stability with respect to oxidation. In Section C, Supporting Information, we report on the work function and change in enthalpy due to oxidation for each proposed metal, to serve as an initial indication of each metal's tendency to oxidize. AlCu<sub>3</sub> is predicted to have a rate of oxidation comparable to Al. ZnGa<sub>3</sub> is found to be more prone to oxidation than Al. ZnCu is more prone to oxidation than Al, but further work is required to compare with Al. Further, the DFT calculations of the quality factors assume pure materials with perfect crystals. For metals, there may be disorder, existence of competing alloys, and stoichiometry errors. Each effect will influence a metal's optical response and the ability to control the structure and composition must be considered. Should there be experimental interest in any of these materials, more follow-up work in this direction could be planned for specific materials. However, such an in-depth study is not feasible in a high-throughput context. Computed extinction, absorption, and reflection spectra for planar vacuum-metal interfaces are shown and discussed in Section G, Supporting Information.

### 3.4. Element Substitutions

The machine-learning approach developed here has shown success in identifying high-quality factor plasmonic metals and is useful for rapidly scanning very large chemical spaces. However, it is not guaranteed to identify the highest-quality factor material. Using the model results as a step in narrowing down the search space, we make element-wise substitutions in the proposed AlCu<sub>3</sub>, ZnCu, and ZnGa<sub>3</sub>. The element-wise substitutions consist of substituting atoms of one element with atoms of another element in the same group. By restricting substitutions to the same group, we expect similar bonding and crystal structure due to the number of valence electrons being unchanged. We make the approximation that the crystal symmetry groups are unchanged by the substitutions, to isolate the effect of changing the chemical composition from effects due to a change in crystal structure and we expect to find similar band structures and optical transitions. Lattice constants and all atomic positions within the unit cells are then relaxed. The materials considered are further limited to those that are available in the Materials Project database.

For AlCu<sub>3</sub> the considered materials are AlAg<sub>3</sub>, AlAu<sub>3</sub>, GaCu<sub>3</sub>, GaAg<sub>3</sub>, InCu<sub>3</sub>, InAg<sub>3</sub>, and InAu<sub>3</sub>. Their quality factors are compared in **Figure 11** and we find that AlCu<sub>3</sub> outperforms all materials in its family up to 2.3 eV for  $Q_{\text{LSPR}}^{\text{DFT}}$  and up to 1.9 eV for  $Q_{\text{SPP}}^{\text{DFT}}$ . At 2.807 eV, all materials in this group display larger  $Q_{\text{LSPR}}^{\text{DFT}}$  and  $Q_{\text{SPP}}^{\text{DFT}}$  values than Au. AlCu<sub>3</sub> displays the largest plasma frequency of 9.00 eV of the substitutions. The plasma frequencies of the remaining materials range from 7.00 eV for GaAg<sub>3</sub> up to 8.51 eV for GaCu<sub>3</sub>. The examined substitutions for ZnCu are ZnAg, ZnAu, CdAg, CdAu, and HgAg, and their quality factors are compared in **Figure 12**. Among these, ZnAg and CdAg

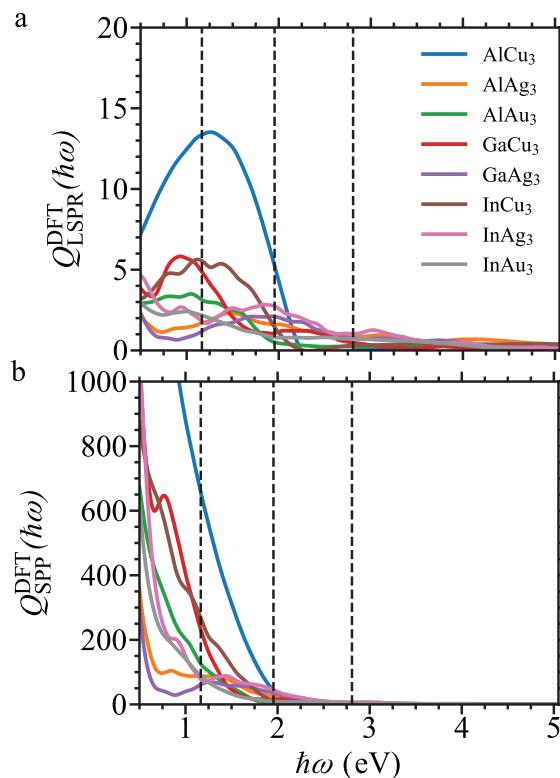


**Figure 11.** Comparison of a)  $Q_{\text{LSPR}}^{\text{DFT}}$  and b)  $Q_{\text{SPP}}^{\text{DFT}}$  for family-substituted AlCu<sub>3</sub> materials.

show the most similar behavior of  $Q_{\text{LSPR}}^{\text{DFT}}$  and  $Q_{\text{SPP}}^{\text{DFT}}$  compared to ZnCu, with a single smooth maximum between 1.0 and 1.4 eV. Finally, the considered substitution materials for ZnGa<sub>3</sub> are ZnAl<sub>3</sub>, ZnIn<sub>3</sub>, CdAl<sub>3</sub>, CdIn<sub>3</sub>, HgGa<sub>3</sub>, and HgIn<sub>3</sub>. Their quality factors are compared in **Figure 13** and they show a more intricate dependence on energy, with ZnAl<sub>3</sub> and CdAl<sub>3</sub> outperforming ZnGa<sub>3</sub>. ZnAl<sub>3</sub> and CdAl<sub>3</sub> are found to have plasma frequencies of 11.67 and 11.08 eV, respectively, both larger than that of ZnGa<sub>3</sub> of 10.64 eV.

In particular for ZnAl<sub>3</sub> and CdAl<sub>3</sub>, the quality factors show strong oscillations with frequency (see **Figure 13a,b**). These oscillations cause the choice of best plasmonic material among the considered group to be strongly dependent on the operating energy. To analyze this more, **Figure 14a** plots the real and imaginary components of the dielectric functions for ZnGa<sub>3</sub>, ZnAl<sub>3</sub>, and CdAl<sub>3</sub> including both the interband and intraband contributions. **Figure 14b** includes only contributions to the dielectric function from interband transitions. This shows that oscillations in real and imaginary part of the frequency-dependent dielectric function of ZnAl<sub>3</sub> and CdAl<sub>3</sub> lead to the oscillations seen in the quality factors.

In summary, element substitutions provide an effective method to extend the search for high-quality factor metals. In the ZnCu family, CdAu and HgAg were found to have higher  $Q_{\text{LSPR}}^{\text{DFT}}$  and  $Q_{\text{SPP}}^{\text{DFT}}$  than ZnCu at 2.8075 eV. In this case though, the two higher-quality factor materials contain toxic Cd and Hg. In the ZnGa<sub>3</sub> family, the metals ZnAl<sub>3</sub> and CdAl<sub>3</sub> are computed to have higher  $Q_{\text{LSPR}}^{\text{DFT}}$  and  $Q_{\text{SPP}}^{\text{DFT}}$  than ZnGa<sub>3</sub> at 1.065, 1.959, and

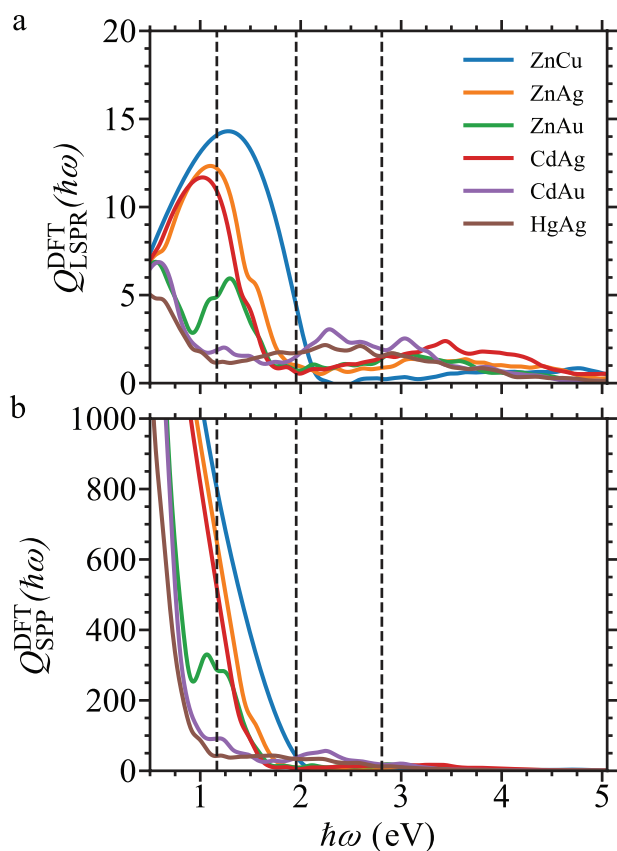


**Figure 12.** Comparison of a)  $Q_{\text{LSPR}}^{\text{DFT}}$  and b)  $Q_{\text{SPP}}^{\text{DFT}}$  for family-substituted ZnCu materials.

2.807 eV. In addition, for ZnAl<sub>3</sub> and CdAl<sub>3</sub> we observe energy-dependent oscillations in the quality factors. The oscillations cause the choice of material to become dependent on the energy of the application.

### 3.5. Decomposing Quality Factors

In the following, we individually analyze interband and intraband contributions to show that both contribute to differences in the quality factor. We note that both contributions combine nonlinearly in the quality factor through the dielectric functions

$$Q_{\text{LSPR}} = -\frac{\epsilon_{1,\text{inter}} + \epsilon_{1,\text{intra}}}{\epsilon_{2,\text{inter}} + \epsilon_{2,\text{intra}}} \quad (12)$$

In **Figure 15** we show the interband (a) and intraband (b) contributions to the quality factor for Ag and the newly proposed AlCu<sub>3</sub>. The behavior for the two metals varies strongly at low energies, corresponding to different sets of allowed optical interband transitions, see **Figure 15a**. The origin of this difference is displayed most prominently in **Figure 10a,b**. At low energies, AlCu<sub>3</sub> allows a small number of optical interband transitions, while Ag has an interband gap. In the UV range, both Ag and AlCu<sub>3</sub> show an increasing number of interband transitions with relative oscillator strengths  $>10^{-3}$ , causing the quality factor for both materials to fall toward 0 in the UV. As a

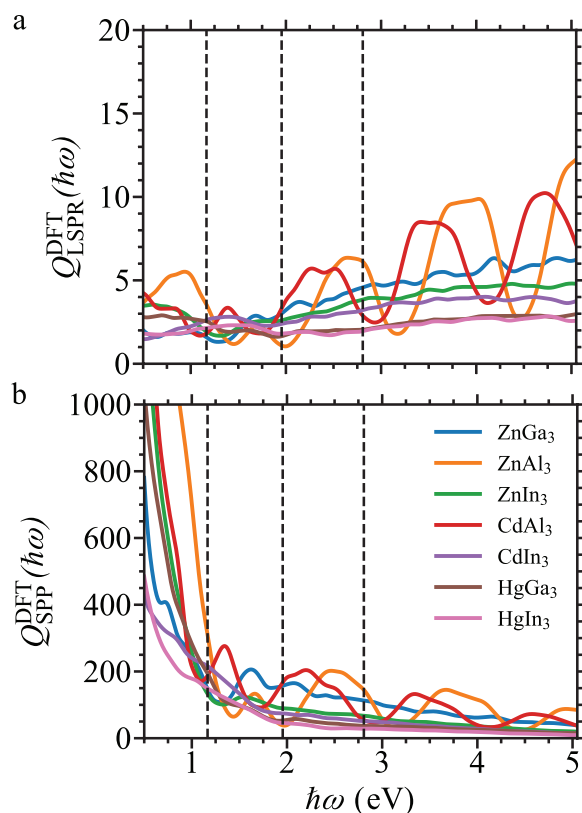


**Figure 13.** Comparison of a)  $Q_{\text{LSPR}}^{\text{DFT}}$  and b)  $Q_{\text{SPP}}^{\text{DFT}}$  for family-substituted ZnGa<sub>3</sub> materials.

result, Ag and AlCu<sub>3</sub> perform better as plasmonic materials in the IR and visible energy ranges than in the UV range.

The intraband contribution depends on material only through the value of the electron relaxation time  $\tau$  and the plasma frequency  $\omega_p^{\text{DFT}}$ . Ag and AlCu<sub>3</sub> are computed to have similar plasma frequencies, 8.96 and 9.00 eV, respectively, hence, appreciable differences in intraband contributions must be a result of differences in  $\tau$ . In metals typical values of  $\tau$  can vary over an order of magnitude, with computation of  $\tau$  for large numbers of materials being prohibitively expensive. Johnson and Christy<sup>[12]</sup> report electron relaxation times for noble metals ranging from 6.9 to 31 fs. In **Figure 16** and **Figure S3**, Supporting Information, we show how the quality factors of Ag depend on  $\tau$  at three different representative energies. As expected, the dependence is strong in the low energy range, that lies within the optical gap of Ag, as there are no interband contributions. At higher energies, this dependence on  $\tau$  disappears, which corresponds to the Drude model becoming transparent in the UV region of the optical spectrum, while interband transitions become the dominant contribution to the dielectric function.

When computing quality factors for the entire dataset of metals in this work, we used a single value of  $\tau = 10$  fs to represent electron relaxation time. Increasing  $\tau$ , corresponding to weaker scattering of oscillating electrons, causes the quality factor to increase with  $\tau$  and the energy of the maximum to redshift, as shown for Ag and AlCu<sub>3</sub> in **Figure 15c**. In AlCu<sub>3</sub>, the maximum quality factor is shifted from 1.286 eV at  $\tau = 6.9$  fs



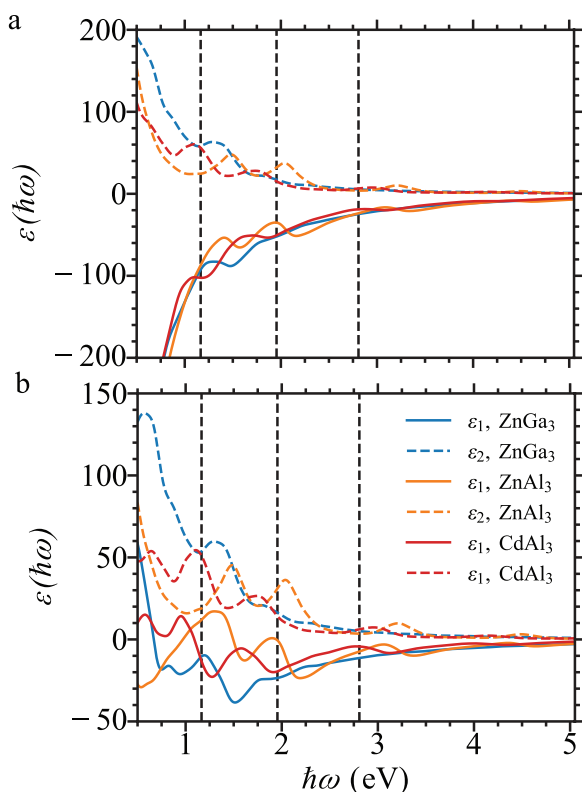


**Figure 14.** a) Real and imaginary parts of the dielectric functions (interband and intraband contributions included) of ZnGa<sub>3</sub>, ZnAl<sub>3</sub>, and CdAl<sub>3</sub>. b) Real and imaginary parts of the dielectric functions of ZnGa<sub>3</sub>, ZnAl<sub>3</sub>, and CdAl<sub>3</sub>, including only the interband contributions.

to 1.112 eV at  $\tau = 31$  fs. The shift of the maximum is more pronounced in Ag, from 1.778 eV at  $\tau = 6.9$  fs to 1.542 eV at  $\tau = 31$  fs. The magnitude of the red-shift is material dependent, based on the interband contributions. The increase in the total quality factor is due only to the increase in the intraband contribution as the electron relaxation time does not influence the interband optical transitions. Definitely choosing between materials would require measuring or computing  $\tau$ . In Section D, Supporting Information, we describe the method for calculating the phonon contribution to  $\tau$ , plot the temperature-dependent  $\tau_{\text{el-ph}}$ , and discuss the consequences. We find that AlCu<sub>3</sub>, ZnCu, and ZnGa<sub>3</sub> all have significantly shorter relaxation times than Ag over the temperature range of 200 to 1000 K. This causes the  $Q_{\text{LSPR}}$  and  $Q_{\text{SPP}}$  values of AlCu<sub>3</sub> and ZnCu at 1.1655 and 1.9590 eV no longer to be competitive with Ag. However, ZnGa<sub>3</sub> remains a viable choice for a UV plasmonic metal.

The influence of  $\tau$  on the position of the quality factor maximum is examined more definitively in Figure 16. In Ag, varying  $\tau$  between 1 and 100 fs smoothly shifts the position of the maximum from 1.88 to 1.30 eV. In AlCu<sub>3</sub>, varying  $\tau$  over the same range shifts the maximum between 1.41 and 0.85 eV. AlCu<sub>3</sub> has a discontinuous jump in the position between  $\tau = 59$  and 60 fs (see detailed discussion in the Supporting Information). This provides a method of manipulating the quality factor in addition to choice of material.  $\tau$  can be altered by controlling the defect density and grain

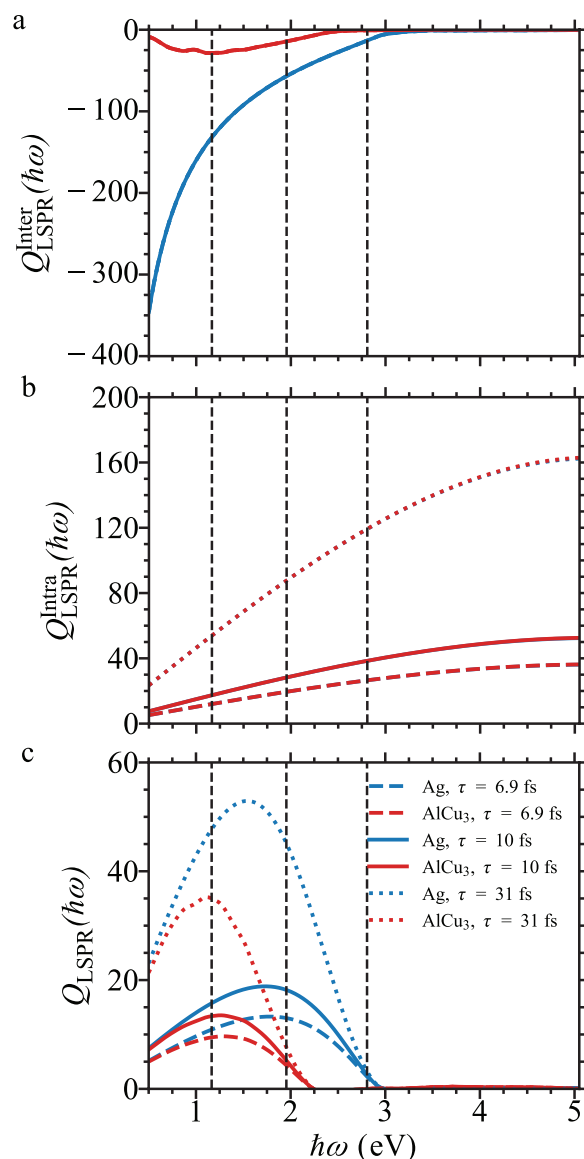


**Figure 15.** Quality factor calculated including only the dielectric function due to a) interband transitions, b) intraband transitions, and c) both interband and intraband contributions. The dielectric functions are evaluated with three experimental relaxation times from Johnson.<sup>[12]</sup>

size. A material's performance as a plasmonic can then be improved through shifting the peak in quality factor to match the operating energy.

## 4. Conclusions

We trained machine-learning models on quality factors derived from dielectric functions that we computed within DFT, to expedite the discovery of new plasmonic materials. Training and testing results for these machine-learning models were discussed and we concluded that they are limited by errors that are of the same order of magnitude as typical quality factors. However, the models still act as a layer of filtering for downselecting

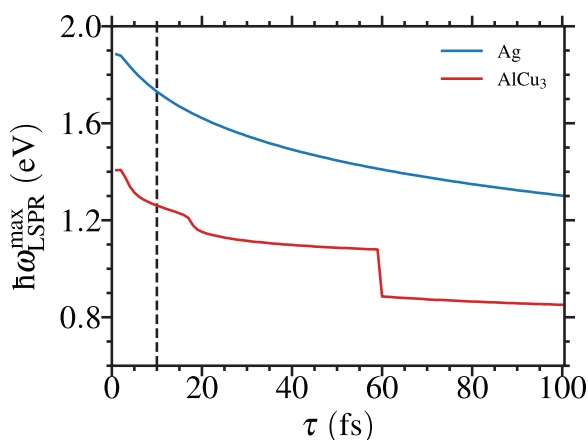


**Figure 16.** Energy of the LSPR quality factor maximum for Ag and AlCu<sub>3</sub> with varying electron relaxation time  $\tau$ . The black dashed vertical line marks the  $\tau = 10$  fs used throughout the previous sections of this paper.

potential high-quality factor materials out of a large pool of candidates on Materials Project. Three particularly promising materials were manually selected for further analysis, AlCu<sub>3</sub>, ZnCu, and ZnGa<sub>3</sub>. We find that allowed optical interband transitions, plasma frequency, and electronic relaxation time all have non-negligible influence on the quality factor across the IR and optical energy ranges.

Of the materials identified by machine learning, AlCu<sub>3</sub> and ZnCu show similar optical behavior to noble metals that are widely used for plasmonics, with a lack of low energy direct interband transitions. In contrast, ZnGa<sub>3</sub> has strong optical transitions in the IR and visible spectral range but weaker absorption in the UV, rendering it a potential UV plasmonic metal. By performing element-wise family substitutions on ZnGa<sub>3</sub>, two more potential UV plasmonic materials have been identified, ZnAl<sub>3</sub> and CdAl<sub>3</sub>. Since in the UV range interband transitions dominate, these results are not affected by the relaxation time. Finally, the machine-learning models demonstrate mixed success in identifying new materials with high plasmonic quality factors at optical energies. Assuming electron relaxation times of 10 fs for all metals, ZnCu outperforms Au at excitation energies of 1.165 and 1.959 eV while AlCu<sub>3</sub> outperforms Au at 1.959 eV. However, Ag shows higher-quality factors than all other considered materials at excitation energies of 1.165 and 1.959 eV for electron relaxation times of both 10 and 31 fs. Nevertheless, despite having similar quality factors AlCu<sub>3</sub> and ZnCu may still be of interest as they are composed of lower cost metals than Au and Ag.

The metals Ag, Au, and Cu function well as plasmonics in the IR and visible energy ranges because they have optical band gaps near 2 eV. For optical excitations between 0 eV and their respective optical gaps, these materials have no interband transitions and the response is described well by the Drude model. This same property is seen in AlCu<sub>3</sub> and ZnCu. However, optical interband transitions in Ag, Au, Cu, AlCu<sub>3</sub>, and ZnCu lead to losses in the UV energy range. Consequently, these materials are not suitable as UV plasmonics. Our approach has identified ZnGa<sub>3</sub> as a potential UV plasmonic material. ZnGa<sub>3</sub>

shows strong optical transitions at low energies, with weaker optical transitions in the UV energy range.

The framework used here is general and can be extended toward any property calculable from the optical dielectric function for both metals and semiconductors in the future. The applicability is most limited by approximating the relaxation time as independent of material choice. While there is limited experimental literature measuring the relaxation time of metals, computing this quantity is expensive and the value is dependent on the quality of real material samples. Hence, explicit first-principles simulations of the electronic relaxation time were not performed here, but we note that controlling sample defects allows a limited amount of control over the energy position of the peak plasmonic quality factor through the relaxation time for a fixed choice of material. Increasing  $\tau$  by removing sample defects may provide a method to red-shift the peak in quality factor while decreasing  $\tau$  by introducing defects blue-shifts the peak, allowing one to better match the operating energy.

## Supporting Information

Supporting Information is available from the Wiley Online Library or from the author.

## Acknowledgements

This material is based upon work supported by the National Science Foundation under grant no. DMR-1555153. This research was part of the Blue Waters sustained-petascale computing project, which was supported by the National Science Foundation (awards OCI-0725070 and ACI-1238993) and the state of Illinois. Blue Waters is a joint effort of the University of Illinois at Urbana-Champaign and its National Center for Supercomputing Applications. This work made use of the Illinois Campus Cluster, a computing resource that is operated by the Illinois Campus Cluster Program (ICCP) in conjunction with the National Center for Supercomputing Applications (NCSA) and which was supported by funds from the University of Illinois at Urbana-Champaign. Further computational resources have been provided by the TU Graz dCluster.

## Conflict of Interest

The authors declare no conflict of interest.

## Data Availability Statement

The data that support the findings of this study are openly available in the Materials Data Facility at <https://doi.org/10.18126/9uxi-x3ft>.

## Keywords

high throughput, machine learning, plasmonics

Received: January 22, 2022

Revised: April 16, 2022

Published online: August 4, 2022

- [1] M. G. Blaber, M. D. Arnold, M. J. Ford, *J. Phys.: Condens. Matter* **2009**, *21*, 144211.
- [2] M. Fox, *Am. J. Phys.* **2002**, *70*, 1269.
- [3] S. A. Maier, P. G. Kik, H. A. Atwater, S. Meltzer, E. Harel, B. E. Koel, A. A. G. Requicha, *Nat. Mater.* **2003**, *2*, 229.
- [4] S. A. Maier, H. A. Atwater, *J. Appl. Phys.* **2005**, *98*, 011101.
- [5] D. P. Fromm, A. Sundaramurthy, P. J. Schuck, G. Kino, W. E. Moerner, *Nano Lett.* **2004**, *4*, 957.
- [6] S. Prayakarao, B. Mendoza, A. Devine, C. Kyaw, R. B. van Dover, V. Liberman, M. A. Noginov, *Appl. Phys. Lett.* **2016**, *109*, 061105.
- [7] S. Kawata, A. Ono, P. Verma, *Nat. Photonics* **2008**, *2*, 438.
- [8] N. Engheta, A. Salandrino, A. Alù, *Phys. Rev. Lett.* **2005**, *95*, 095504.
- [9] N. Engheta, *Science* **2007**, *317*, 1698.
- [10] T. Stakenborg, L. Lagae, *Appl. Phys. Lett.* **2012**, *100*, 173114.
- [11] J. B. Khurgin, A. Boltasseva, *MRS Bull.* **2012**, *37*, 768.
- [12] P. B. Johnson, R. W. Christy, *Phys. Rev. B* **1972**, *6*, 4370.
- [13] M. A. Ordal, R. J. Bell, R. W. Alexander, L. L. Long, M. R. Querry, *Appl. Opt.* **1985**, *24*, 4493.
- [14] E. J. Zeman, G. C. Schatz, *J. Phys. Chem.* **1987**, *91*, 634.
- [15] M. Kanehara, H. Koike, T. Yoshinaga, T. Teranishi, *J. Am. Chem. Soc.* **2009**, *131*, 17736.
- [16] J. Gómez Rivas, M. Kuttge, H. Kurz, P. Haring Bolivar, J. Sánchez-Gil, *Appl. Phys. Lett.* **2006**, *88*, 082106.
- [17] T. D. Neal, K. Okamoto, A. Scherer, *Opt. express* **2005**, *13*, 5522.
- [18] T. P. Sidiropoulos, R. Röder, S. Geburt, O. Hess, S. A. Maier, C. Ronning, R. F. Oulton, *Nat. Phys.* **2014**, *10*, 870.
- [19] W. Kohn, L. J. Sham, *Phys. Rev.* **1965**, *140*, A1133.
- [20] A. Jain, S. P. Ong, G. Hautier, W. Chen, W. D. Richards, S. Dacek, S. Cholia, D. Gunter, D. Skinner, G. Ceder, K. A. Persson, *APL Mater.* **2013**, *1*, 011002.
- [21] R. H. Taylor, F. Rose, C. Toher, O. Levy, K. Yang, M. B. Nardelli, S. Curtarolo, *Comp. Mater. Sci.* **2014**, *93*, 178.
- [22] J. E. Saal, S. Kirklin, M. Aykol, B. Meredig, C. Wolverton, *JOM* **2013**, *65*, 1501.
- [23] C. Ortiz, O. Eriksson, M. Klintonberg, *Comput. Mater. Sci.* **2009**, *44*, 1042.
- [24] G. Bergerhoff, I. Brown, F. Allen, in *Crystallographic Databases*, International Union of Crystallography, Chester, UK **1987**, pp. 77–95.
- [25] M. Scheffler, C. Draxl, *The NOMAD Repository*, Max Planck Computer & Data Facility, Garching, Germany **2014**.
- [26] W. Setyawan, R. M. Gaume, S. Lam, R. S. Feigelson, S. Curtarolo, *ACS Comb. Sci.* **2011**, *13*, 382.
- [27] K. M. Poduska, L. Regev, E. Boaretto, L. Addadi, S. Weiner, L. Kronik, S. Curtarolo, *Adv. Mat.* **2011**, *23*, 550.
- [28] A. M. Deml, R. O'Hayre, C. Wolverton, V. Stevanović, *Phys. Rev. B* **2016**, *93*, 085142.
- [29] M. N. Obrovac, V. L. Chevrier, *Chem. Rev.* **2014**, *114*, 11444.
- [30] J. Greeley, T. Jaramillo, J. Bonde, I. Chorkendorff, J. Nørskov, *Nat. Mater.* **2006**, *5*, 909.
- [31] L. Yu, A. Zunger, *Phys. Rev. Lett.* **2012**, *108*, 068701.
- [32] E. P. Shapera, A. Schleife, *Adv. Theory Simul.* **2018**, *1*, 1800075.
- [33] L. M. Ghiringhelli, J. Vybiral, S. V. Levchenko, C. Draxl, M. Scheffler, *Phys. Rev. Lett.* **2015**, *114*, 105503.
- [34] P. West, S. Ishii, G. Naik, N. Emani, V. Shalaev, A. Boltasseva, *Laser Photonics Rev.* **2010**, *4*, 795.
- [35] M. W. Knight, T. Coenen, Y. Yang, B. J. M. Brenny, M. Losurdo, A. S. Brown, H. O. Everitt, A. Polman, *ACS Nano* **2015**, *9*, 2049.
- [36] E. G. Maksimov, I. I. Mazin, S. N. Rashkeev, Y. A. Uspenski, *J. Phys. F: Met. Phys.* **1988**, *18*, 833.
- [37] M. Kumar, N. Umezawa, S. Ishii, T. Nagao, *ACS Photonics* **2016**, *3*, 43.
- [38] A. Catellani, A. Calzolari, *Phys. Rev. B* **2017**, *95*, 115145.
- [39] M. Bernardi, J. Mustafa, J. B. Neaton, S. G. Louie, *Nat. Commun.* **2015**, *6*, 7044.
- [40] R. Binder, H. S. Köhler, M. Bonitz, N. Kwong, *Phys. Rev. B* **1997**, *55*, 5110.
- [41] F. Ladstädter, U. Hohenester, P. Puschnig, C. Ambrosch-Draxl, *Phys. Rev. B* **2004**, *70*, 235125.
- [42] J. Y. Seto, *J. Appl. Phys.* **1975**, *46*, 5247.
- [43] G. Baccarani, B. Ricco, G. Spadini, *J. Appl. Phys.* **1978**, *49*, 5565.
- [44] A. Kronenberger, A. Polity, D. M. Hofmann, B. K. Meyer, A. Schleife, F. Bechstedt, *Phys. Rev. B* **2012**, *86*, 115334.
- [45] S. Zhang, B. Xu, Y. Lin, C. Nan, W. Liu, arXiv:1710.02495, **2017**.
- [46] G. Kresse, J. Furthmüller, *Phys. Rev. B* **1996**, *54*, 11169.
- [47] G. Kresse, D. Joubert, *Phys. Rev. B* **1999**, *59*, 1758.
- [48] M. Gajdoš, K. Hummer, G. Kresse, J. Furthmüller, F. Bechstedt, *Phys. Rev. B* **2006**, *73*, 045112.
- [49] P. Hahn, W. Schmidt, F. Bechstedt, *Phys. Rev. Lett.* **2001**, *88*, 016402.
- [50] F. Fuchs, C. Roedel, A. Schleife, F. Bechstedt, *Phys. Rev. B* **2008**, *78*, 085103.
- [51] C. McGahan, K. Appavoo, R. F. Haglund Jr, E. P. Shapera, *J. Vac. Sc. Technol. B: Nanotechnol. Microelectron.* **2013**, *31*, 06FE01.
- [52] J. I. Ziegler, R. F. Haglund Jr, *Nano Lett.* **2010**, *10*, 3013.
- [53] J. A. Hachtel, R. B. Davidson, E. R. Kovalik, S. T. Retterer, A. R. Lupini, R. F. Haglund, B. J. Lawrie, S. T. Pantelides, *Opt. Lett.* **2018**, *43*, 927.
- [54] T. Corrigan, P. Kolb, A. Sushkov, H. Drew, D. Schmadel, R. Phaneuf, *Opt. Express* **2008**, *16*, 19850.
- [55] S. Tunsiri, N. Thammawongsa, T. Threepak, S. Mitatha, P. Yupapin, *Plasmonics* **2019**, *14*, 1669.
- [56] K. Mcpeak, S. Jayanti, S. Kress, S. Meyer, S. Iotti, A. Rossinelli, D. J. Norris, *ACS Photonics* **2015**, *2*, 150203150623003.
- [57] A. Jain, S. P. Ong, G. Hautier, W. Chen, W. D. Richards, S. Dacek, S. Cholia, D. Gunter, D. Skinner, G. Ceder, K. a. Persson, *APL Mater.* **2013**, *1*, 011002.
- [58] S. P. Ong, W. D. Richards, A. Jain, G. Hautier, M. Kocher, S. Cholia, D. Gunter, V. L. Chevrier, K. A. Persson, G. Ceder, *Comput. Mater. Sci.* **2013**, *68*, 314.
- [59] G. Montavon, M. Rupp, V. Gobre, A. Vazquez-Mayagoitia, K. Hansen, A. Tkatchenko, K.-R. Müller, O. A. Von Lilienfeld, *New J. Phys.* **2013**, *15*, 095003.
- [60] A. P. Bartók, S. De, C. Poelking, N. Bernstein, J. R. Kermode, G. Csányi, M. Ceriotti, *Scie. Adv.* **2017**, *3*, e1701816.
- [61] D. Bonchev, *Chemical Graph Theory: Introduction and Fundamentals*, Vol. 1, CRC Press, Boca Raton, FL **1991**.
- [62] L. Mentel, mendelev – A python resource for properties of chemical elements, ions and isotopes, <https://bitbucket.org/lukaszmentel/mendelev>.
- [63] F. Pedregosa, G. Varoquaux, A. Gramfort, V. Michel, B. Thirion, O. Grisel, M. Blondel, P. Prettenhofer, R. Weiss, V. Dubourg, J. Vanderplas, A. Passos, D. Cournapeau, M. Brucher, M. Perrot, E. Duchesnay, *J. Mach. Learn. Res.* **2011**, *12*, 2825.
- [64] J. P. Perdew, J. A. Chevary, S. H. Vosko, K. A. Jackson, M. R. Pederson, D. J. Singh, C. Fiolhais, *Phys. Rev. B* **1992**, *46*, 6671.
- [65] F. Hajiesmaeilbaigi, A. Motamedi, *Laser Phys. Lett.* **2007**, *4*, 133.
- [66] A. Pyatenko, M. Yamaguchi, M. Suzuki, *J. Phys. Chem. C* **2009**, *113*, 9078.
- [67] A. Parisi, A. C. Cino, A. C. Busacca, M. Cherchi, S. Riva-Sanseverino, *Sensors* **2008**, *8*, 7113.
- [68] A. Lesuffeur, H. Im, N. Lindquist, K. Seop Lim, S.-H. Oh, *Opt. Express* **2008**, *16*, 219.
- [69] I. Khan, H. Keshmiri, F. Kolb, T. Dimopoulos, E. J. W. List-Kratochvil, J. Dostalek, *Adv. Opt. Mater.* **2016**, *4*, 435.
- [70] A. Neogi, S. Karna, R. Shah, U. Phillipose, J. Perez, R. Shimada, Z. M. Wang, *Nanoscale* **2014**, *6*, 11310.
- [71] B. Blaiszik, K. Chard, J. Pruyne, R. Ananthkrishnan, S. Tuecke, I. Foster, *JOM* **2016**, *68*, 2045.

- [72] B. Blaiszik, L. Ward, M. Schwarting, J. Gaff, R. Chard, D. Pike, K. Chard, I. Foster, arXiv:1904.10423, **2019**.
- [73] E. Shapera, A. Schleife, Dataset for the paper “discovery of new plasmonic metals via high throughput machine learning”, **2021**, [https://petreldata.net/mdf/detail/shapera\\_paper\\_discovery\\_learning\\_v1.1](https://petreldata.net/mdf/detail/shapera_paper_discovery_learning_v1.1).
- [74] Y. Dodge, *The concise encyclopedia of statistics*, Springer Science & Business Media, Cham **2008**.
- [75] A. Seko, A. Togo, I. Tanaka, *Nanoinformatics*, Springer, Singapore **2018**, pp. 3–23.
- [76] H. Moriwaki, Y.-S. Tian, N. Kawashita, T. Takagi, *J. Cheminf.* **2018**, *10*, 41.
- [77] G. Landrum, *RDKit Documentation, Release 1*, **2013**, pp. 1–79.
- [78] K. T. Butler, D. W. Davies, H. Cartwright, O. Isayev, A. Walsh, *Nature* **2018**, *559*, 547.
- [79] J. Carrasquilla, R. G. Melko, *Nat. Phys.* **2017**, *13*, 431.
- [80] M. H. Segler, M. Preuss, M. P. Waller, *Nature* **2018**, *555*, 604.
- [81] R. Gómez-Bombarelli, J. Aguilera-Iparraguirre, T. D. Hirzel, D. Duvenaud, D. Maclaurin, M. A. Blood-Forsythe, H. S. Chae, M. Einzinger, D.-G. Ha, T. Wu, G. Markopoulos, *Nat. Mater.* **2016**, *15*, 1120.
- [82] G. Hepner, T. Logan, N. Ritter, N. Bryant, *Photogramm. Eng. Remote Sens.* **1990**, *56*, 469.
- [83] G. Foody, M. McCulloch, W. Yates, *Int. J. Remote Sens.* **1995**, *16*, 1707.
- [84] A. Habib, F. Florio, R. Sundararaman, *J. Opt.* **2018**, *20*, 064001.
- [85] Y. Hinuma, G. Pizzi, Y. Kumagai, F. Oba, I. Tanaka, *Comput. Mater. Sci.* **2017**, *128*, 140.
- [86] A. Togo, I. Tanaka, arXiv:1808.01590, **2018**.
- [87] J. P. Perdew, K. Burke, Y. Wang, *Phys. Rev. B* **1996**, *54*, 16533.
- [88] V. I. Anisimov, F. Aryasetiawan, A. Lichtenstein, *J. Phys.: Condens. Matter* **1997**, *9*, 767.
- [89] J. Heyd, G. E. Scuseria, M. Ernzerhof, *J. Chem. Phys.* **2003**, *118*, 8207.
- [90] J. Heyd, G. E. Scuseria, M. Ernzerhof, *J. Chem. Phys.* **2006**, *124*, 219906.